RESEARCH ARTICLE

Macromolecular Materials and Engineering
www.mame-journal.de

Enzyme-Induced Ferrification of Hydrogels for Toughening of Functional Inorganic Compounds

*Marko Milovanovic, Nicolas Rauner, Emre Civelek, Tim Holtermann, Oualid El Jid, Monika Meuris, Volker Brandt, and Joerg C. Tiller**

Enzyme-induced mineralization (EIM) has been shown to greatly enhance the mechanical properties of hydrogels by precipitation of calcium salts. Another feature of such hydrogels is their high toughness even when containing finely nanostructured mineral content of ≈75 wt%. This might be useful for bendable materials with high content of functional inorganic nanostructures. The present study demonstrates that EIM can form homogeneous nanostructures of water-insoluble iron salts within hydrogels. Crystalline iron(II) carbonate precipitates urease-induced within polyacrylate-based hydrogels and forms platelet structures that have the potential of forming self-organized nacre-like architectures. The platelet structure can be influenced by chemical composition of the hydrogel. Further, amorphous iron(II) phosphate precipitates within hydrogels with alkaline phosphatase, forming a nanostructured porous inorganic phase, homogeneously distributed within the double network hydrogel. The high amount of iron phosphate (more than 80 wt%) affords a stiffness of ≈100 MPa. The composite is still bendable with considerable toughness of 400 J m^{-2} and strength of 1 MPa. The high water content (>50%) may allow fast diffusion processes within the material. This makes the iron phosphate-based composite an interesting candidate for flexible electrodes and demonstrates that EIM can be used to deliberately soften ceramic materials, rendering them bendable.

1. Introduction

Modern high performance biomaterials frequently derive their superior performance from different nanostructured phases, which combine their individual properties often synergistically within one material. Purely organic materials, for instance amphiphilic polymer conetworks (APCN), combine two polymer nanophases with orthogonal swelling properties, resulting in fully transparent materials that swell in orthogonal solvents.[1–8] A similar concept is also known from double network hydrogels (DNH), which combine two polymer networks – one usually being higher cross-linked, while the second, loosely cross-linked network provides stretchability – with sacrificial bonds that become orders of magnitude stiffer and stronger than the respective single polymer network.[9–13] Nature has employed reinforcing mechanisms in cartilage by forming a DNH of collagen and hyaluronic acid.[14–15] Further, the combination of organic and inorganic materials is found in nacre and in bones, both of them showing greatly improved toughness of the stiffening ceramic component by combining it with an organic nanophase.[16–18] Recently, this remarkable, synergistic behavior has been investigated and applied in the development of synthetic materials, such as artificial nacre.[19–22] The most crucial part, when combining an inorganic and an organic nanophase is the homogenous formation of the inorganic nanostructures within a given polymer matrix. For example, $CaCO_3$ crystals can be grown inside hydrogels by different diffusion based methods,[23–24] like vapor,[25–27] or counter diffusion[28,29] or with the Kitano[30] or soaking method.[31] Incorporating inorganic fillers is also possible by adding inorganic components[32–38] or their respective precursors, e.g., silanes,[39–41] to monomer/polymer solutions prior to network formation. However, the most prominent problem of all these methods is either the inhomogeneous distribution or an insufficient amount of precipitated inorganic material inside the hydrogel. Further, preparation of nanocomposites can be very time-consuming and elaborate, and often leads to small-scale samples. A recent method to achieve the formation of highly ordered nanostructures within a polymer matrix is the enzyme-induced mineralization (EIM).[42–47] This method allows the formation of percolated nanostructures of amorphous and crystalline calcium carbonate and -phosphate within hydrogels. The degree of mineralization of such materials reaches 70–90 wt%, and the fully transparent materials can be tuned in stiffness over several orders of magnitude while also

M. Milovanovic, N. Rauner, E. Civelek, T. Holtermann, O. E. Jid, M. Meuris, V. Brandt, J. C. Tiller
Biomaterials and Polymer Science
Department of Bio- and Chemical Engineering
TU Dortmund
Emil-Figge-Str. 66, 44227 Dortmund, Germany
E-mail: joerg.tiller@tu-dortmund.de

The ORCID identification number(s) for the author(s) of this article can be found under https://doi.org/10.1002/mame.202200051

DOI: 10.1002/mame.202200051

showing a remarkable toughness, with fracture energies of 1000–2000 J m^{-2}. Thus, the enzyme-induced mineralization can be used to significantly stiffen and strengthen organic hydrogels. However, this method also allows the deliberate softening of inorganic materials, rendering them tougher. Particularly iron salts, such as iron phosphates and carbonates, are interesting candidates for the enzyme-induced mineralization as flexible iron-based composites might lead to the development of new materials, such as bendable batteries,[48] catalytically active membranes,[49] or electrodes.[50–51] The present study investigates the EIM regarding the potential to form ordered iron salt nanostructures homogenously precipitated within hydrogels and how this ferrification might lead to tough and flexible, yet highly filled and functional composite nanomaterials.

2. Results and Discussion

2.1. Urease-Induced Precipitation of $FeCO_3$

Goal of this study was the adaptation of the EIM for iron salts in order to create highly ordered, flexible and tough iron salt nanostructures within a hydrogel. One interesting EIM-system is the precipitation of iron carbonate assisted by the enzyme urease, which catalyzes the hydrolysis of urea and thus locally produces carbonate ions. Therefore, it was first investigated whether urease tolerates iron salts in relevant concentrations, as iron ions are known inhibitors for the enzyme.[52] Since the carbonate of iron(III) is unstable,[53] only iron(II) ions were considered. The experiment was performed in an iron(II) chloride solution stabilized with triethanolamine (TEA) by adding 1 mg urease per 100 mL solution. The solution with concentrations of $FeCl_2$ in a concentration range between 0.14 M and 0.41 without the enzyme is stable between pH 5 and 9.3, i.e., no precipitate is formed within 1 week. The addition of urease to the $FeCl_2$/TEA solution leads to the formation of a white precipitate within 6 h, when the concentration of the iron salt is higher than 0.14 M and lower than 0.41 and the pH is pH 7 or higher. The precipitate was found to be $FeCO_3$ platelets, which is typical for this salt. In order to explore, if the enzyme is truly inhibited at 0.41 M $FeCl_2$, 0.27 M $CaCl_2$ was added to this solution and urease was added. No precipitate is formed in this experiment, while $CaCO_3$ precipitates in the same solution without the iron ions after 30 min. This indicates that urease is fully inhibited at the high iron(II) concentration.

Having established that urease precipitates solids from a Fe(II)Cl_2 containing solution, a network composed of poly(*N*,*N*-dimethylacrylamide) cross-linked by triethylene glycol dimethacrylate (PDMA-*l*-TEG) containing 1 wt% urease (typical for $CaCO_3$ precipitation given previous experience) was added to the above optimized ferrification solution and at 60 °C, the highest applicable temperature for urease.[42–44,46] After 15 min the hydrogel became cloudy and showed a brownish coloration (see **Figure 1**), while control networks without urease stayed clear and colorless even after 7 d of incubation. This indicates that the sole reason for the precipitation of the solid is the presence of urease within the hydrogel.

As seen from the scanning electron microscopy (SEM) images in **Figure 2**, the urease-induced ferrification of the hydrogel network leads to the formation of sub-micrometer structures evenly distributed and precipitated throughout the hydrogel. Sub-micrometer sized platelets are formed with lengths of 0.5–1 µm and a thickness of 50–70 nm, which are partially covered by the polymer matrix. The platelets look similar to those formed in solution, indicating that the polymer matrix does not influence the crystallization within the hydrogel.

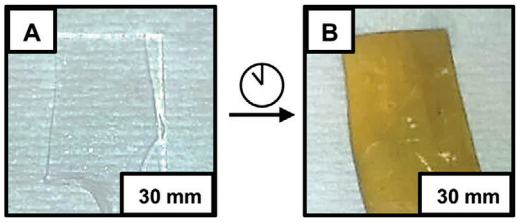

Figure 1. Exemplary image of PDMA-*l*-TEG networks (1 wt% TEG, 1 wt% UF) after preparation and swelling in water A) and after ferrification B) in a TEA buffered (0.2 M, pH 7.5) aqueous solution of $FeCl_2 \cdot 4H_2O$ (53.9 g L^{-1}) and urea (10 g L^{-1}) at 60 °C for 24 h.

Although, the platelets are generally nonordered throughout the majority of the mineralized hydrogel, they form well-ordered brick-like structures around the few enclosed gas bubbles (**Figure 3**). This might be due to the stretching of the polymer chains around the enclosed air bubble, by which the plates orientate themselves during crystal growth. Alternatively, this orientation can also be caused by localized, drying-related shrinking of the hydrogel, which stacks the nanoplatelets on top of one another, similar to architectures achieved with bidirectional freeze casting and hydrogel-film casting.[54,55] The observed structure has a striking resemblance to natural, highly ordered and hierarchical composite materials such as nacre, as comparison shows (cf. Figure 3A–C,D). Unfortunately, this highly ordered structure is only found in the surrounding layers of occasionally occurring gas bubbles.

Further investigations of the precipitated platelets inside the hydrogels using transmission electron microscopy (TEM) and selected area electron diffraction (SAED) measurements revealed that the nanoplatelet structure can be attributed to siderite, a crystalline modification of iron(II) carbonate, which is supported by respective fourier-transform infrared spectroscopy (FTIR) measurements (**Figure 4**C). Energy-dispersive X-ray spectroscopy (TEM-EDX) measurements reveal iron, oxygen, and carbon (Figure 4E), which make up the composition of the inorganic platelets. In combination with respective X-ray diffraction (XRD) measurements (Figure 4D), the crystalline component of the precipitated $FeCO_3$ was assigned to siderite.[56–58]

The ferrified PDMA-*l*-TEG was found to be highly filled with inorganic material (70 wt_{Inorg}%). Although the composite has a fairly high water content (swelling ratio = 2.6) the material breaks at minimal deformation. As found previously, one way to achieve a tough composite hydrogel, the precipitated inorganic material has to form a homogeneous percolated nanophase within the polymer matrix.[42–43,45,59,60] In order to render the platelets into such a phase, it was investigated, if pH has an influence on the formed siderite crystals. Thus, the pH in the ferrification solution was varied between pH 4 and 9.3. As seen in Figure S1 (Supporting Information), the EIM at pH 4 only occurred marginally at the surface of the hydrogel, while the ferrification occurred at all other pH values within the material. The precipitated white substance is typical for $FeCO_3$, while the brown compounds on the

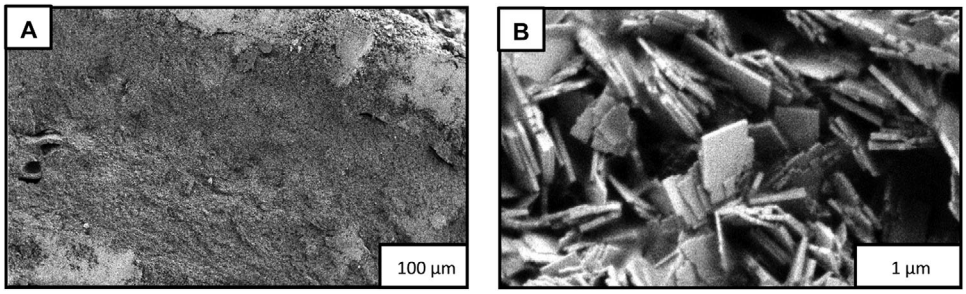

Figure 2. A,B) SEM-images of a PDMA-*l*-TEG cross-section (1 wt% TEG, 1 wt% urease) after ferrification in a TEA buffered (0.2 M, pH 7.5) aqueous solution of $FeCl_2 \bullet 4H_2O$ (53.9 g L^{-1}) and urea (10 g L^{-1}), at 60 °C 24 h. SEM-Images were taken in the middle of the network.

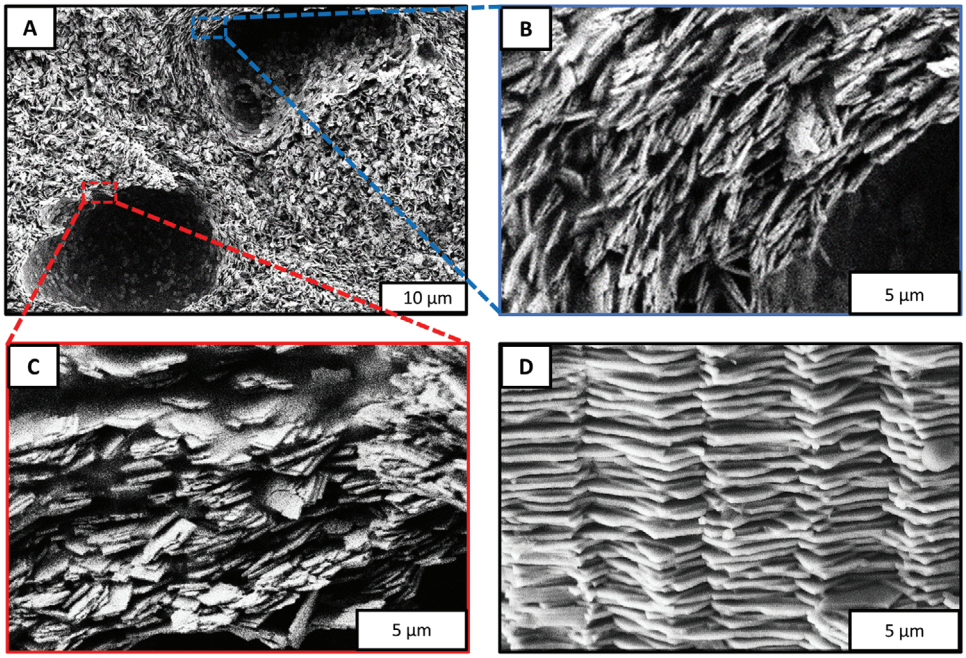

Figure 3. SEM-images of a PDMA-*l*-TEG cross-section (1 wt% TEG, 1 wt% urease) after ferrification in a TEA buffered (0.2 M, pH 7.5) aqueous solution of $FeCl_2$ (53.9 g L^{-1}) and urea (10 g L^{-1}), at 60 °C 24 h. Images were taken in the middle of the film, where air bubbles got trapped during polymerization. D) SEM image of the fracture surface of an abalone shell (cross section) for comparison.

surface can be attributed to the respective oxidized Fe(III) salt. Thus, the hydrogel protects the precipitated $FeCO_3$ from oxidation. Investigation of the precipitated amount of inorganic content reveals that in all cases the $FeCO_3$ precipitated as nonordered platelets of similar size, rendering the material brittle.

Another important influencing factor for tough organic/inorganic hydrogels is to find the percolation point of the inorganic matrix, because beyond this point the inorganic phase renders the material brittle as well.[43,46] Thus, a PDMA-*l*-TEG network with 1 wt% urease was ferrified at 20 and 60 °C, respectively, and samples were taken at regular intervals and examined optically and by SEM, as well as thermogravimetrically.

The stereomicroscopic image shows the formation of a continuous layer just below the surface of the hydrogel after 15 min at 60 °C (**Figure 5**B). Starting from this layer, further $FeCO_3$ forms inside the network, permeating the entire interior of the matrix within 2 h (Figure 5A–F). Figure 5 also shows the mass fraction of the iron carbonate precipitated in the network, plotted against the ferrification time. The dry ferrified network composite consists of equal parts of organic and inorganic components by weight after 45 min. After 6 h at a ferrification temperature of 60 °C, the precipitation of inorganic material slows down and smaller changes in inorganic weight content are observed, reaching almost 70% wt_{Inorg}% after 24 h.

Closer inspection of the formed crystals using SEM correspond to the observations made by stereomicroscopy: At first, the formation of tiny, few nm large, faceted particles can be observed (Figure 5, blue excerpt), which ultimately develop into the iron carbonate platelets within 45 min. The latter do not change even after 24 h of ferrification (Figure 5, red excerpt). Further, a "ferrification front" was observed, which – in accordance to stereomicroscopic images – begins below the surface of the hydrogel and proceeds to grow into the network interior (Figure 5). The respective states of growth of the $FeCO_3$ nanoplatelets change along this gradient during ferrification. The ferrifications appear to be homogeneous after 2 h (Figure 5, SEM images).

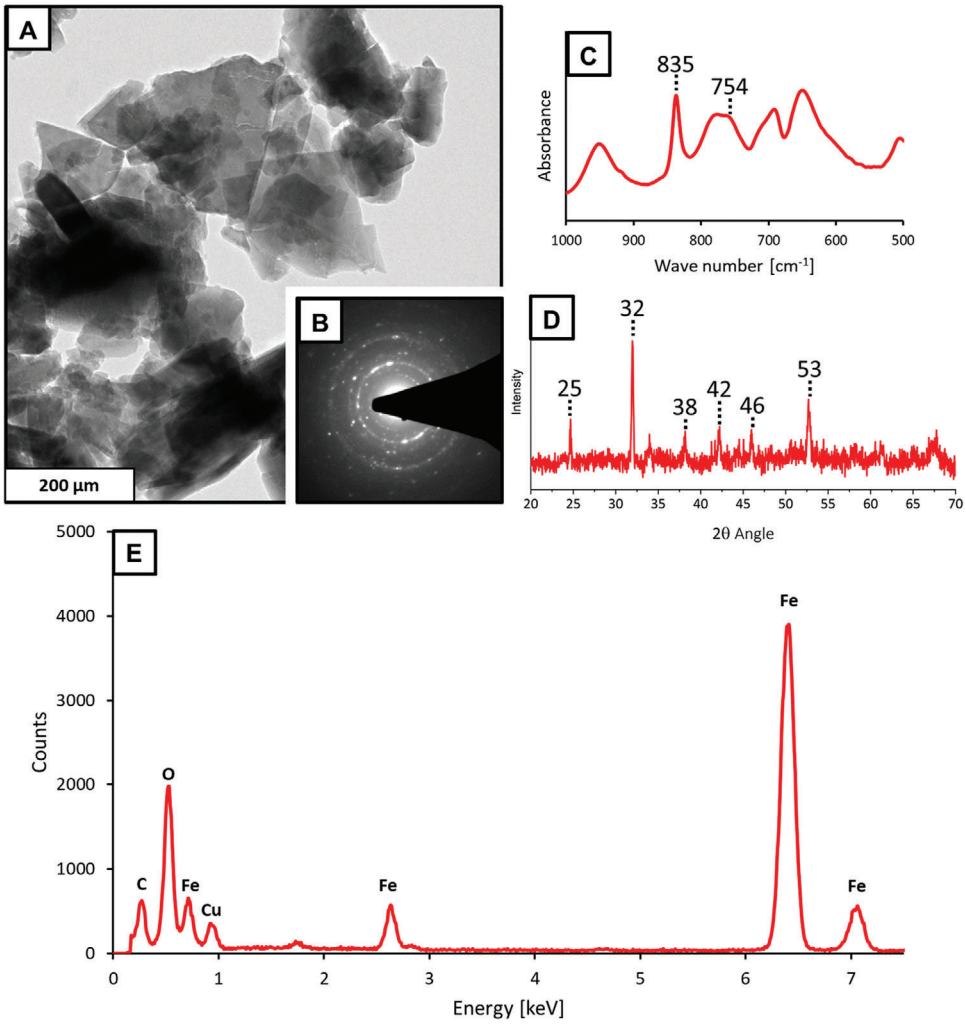

Figure 4. Exemplary TEM image A), SAED image B), FTIR Spectrum C), and XRD pattern D) of the precipitated inorganic plate structures grown in the ferrified PDMA-*l*-TEG conetwork A) (1 wt% TEG, 1 wt% urease) after ferrification in a TEA buffered (0.2 M, pH 7.5) aqueous solution of $FeCl_2 \bullet 4H_2O$ (53.9 g L^{-1}) and urea (10 g L^{-1}) at 60 °C 24 h, with typical SAED images in the right corner B). TEM-EDX pattern of a composite slice recorded on a copper grid E).

The mechanical properties of the composite ferrified at 60 °C are presented in **Figure 6**. Since homogeneous samples are required for mechanical measurement, the first samples was measured after 2 h of ferrification. This sample showed a considerable stiffening compared to the starting hydrogel with the Young´s Modulus increasing from <1 to 4.1 ± 0.4 MPa. After 24 h of mineralization, the Young´s Modulus of the ferrified PDMA-*l*-TEG networks reaches 170 ± 78 MPa. This high increase in stiffness, however, is not associated with a noticeable increase in the inorganic weight content (cf. Figures 5 and 6). This sudden increase might be due to a complete filling of the hydrogel with the $FeCO_3$-nanoplatelets. The calculated fracture energies of the ferrified networks are low. Thus, in these cases, the incorporation of $FeCO_3$ into the hydrogel does not yield a combination of increased stiffness of the hydrogel and increased toughness of the inorganic compound.

One reason for the brittleness of the ferrified hydrogels might be a missing singular percolation point, which is due to the inorganic phase not growing uniformly within the hydrogel (see Figure 5). This results in different densities of the precipitated $FeCO_3$ platelets, rendering the material brittle due to being highly mineralized in some areas, while mineralization is unfinished in others. Obtaining a more homogenous ferrification might be possible by variation urease amount within the hydrogel. To this end, PDMA-*l*-TEG networks with 0.25, 0.5, 2, and 3 wt% urease were ferrified in a TEA buffered ferrification solution (pH 7.5) at 60 °C for 24 h. Urease concentrations lower than 1 wt% led to cloudy ferrification (0.25 wt_{Urease}%) and a patchy (0.5 wt_{Urease}%) material (Figure S2A,B, Supporting Information). Higher amounts of enzyme loading led to the precipitation of inorganic material near the surface, similar to the $FeCO_3$-precipitation observed during the first stages of hydrogel ferrification (cf. Figure 5C–E and cross-section image Figure S2C, Supporting Information), with significantly reduced ferrification deeper inside. This was also observed in previous work in the case of $CaCO_3$-precipitation and is most probably a

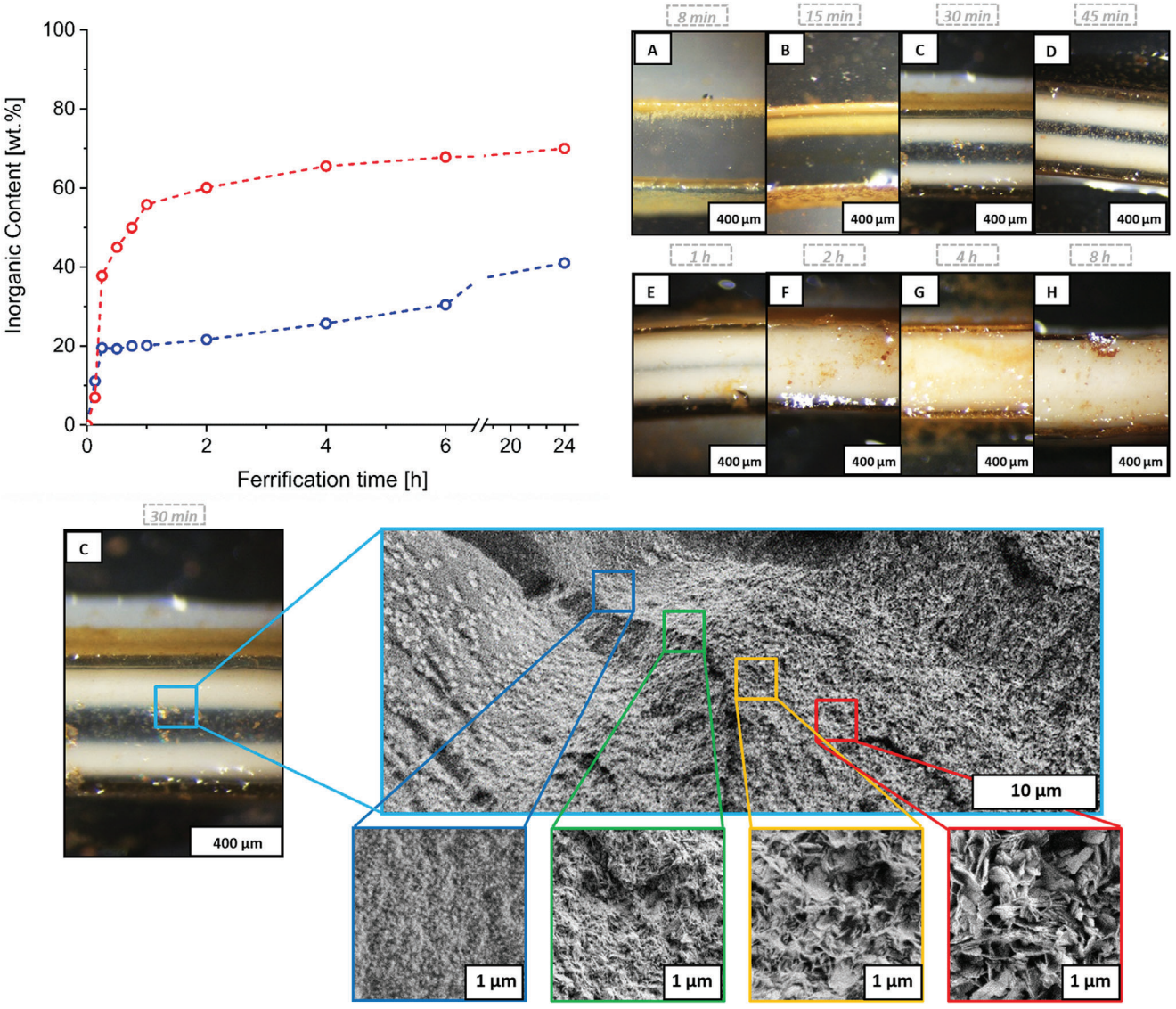

Figure 5. Increase in degree of ferrification (inorganic content wt%) over ferrification time in PDMA-*l*-TEG network (1 wt% TEG, 1 wt% urease) in a TEA buffered (0.2 M, pH 7.5) aqueous solution of $FeCl_2 \cdot 4H_2O$ (53.9 g L^{-1}) and urea (10 g L^{-1}) at 20 °C (blue) and 60 °C (red). Images of a PDMA-*l*-TEG cross-section (1 wt% TEG, 1 wt% urease) after ferrification in a TEA buffered (0.2 M, pH 7.5) aqueous solution of $FeCl_2 \cdot 4H_2O$ (53.9 g L^{-1}) and urea (10 g L^{-1}), at 60 °C after different ferrification times A–G). SEM-images of a PDMA-*l*-TEG cross-section (1 wt% TEG, 1 wt% urease) after ferrification in a TEA buffered (0.2 M, pH 7.5) aqueous solution of $FeCl_2 \cdot 4H_2O$ (53.9 g L^{-1}) and urea (10 g L^{-1}), at 60 °C after different ferrification times at 60 °C for 30 min.

result of dramatically increased urea cleavage at the hydrogel surface, which ultimately leads to fast precipitation of $FeCO_3$ on the surface before the ions can diffuse deeper into the hydrogel.[46] In order to realize a more homogeneous ferrification over time, ferrification was investigated at 20 °C. This way, the reaction rate of the urea hydrolysis decreases, while the diffusion rate is less affected. As expected, the ferrification is slower at 20 °C (Figure 5, blue graph) and first indications of ferrification in the form of white precipitants inhomogenously formed within the network are observable after 4 h, with wt_{Inorg}% reaching a maximum of 41 wt% after 24 h. However, even this slowed reaction rate does not lead to a more homogeneous precipitation (Figure 3, Supporting Information). Further, ferrification experiments at 30, 40, and 50 °C were conducted for 24 h (**Table 1**). However, while temperature influence was observable, the hydrogels either increased in stiffness, but became brittle (40–60 °C) or did not show any significant stiffening at all (20–30 °C).

Thus, the precipitation of $FeCO_3$ platelets cannot be used to obtain a flexible hydrogel highly filled with this iron salt. To avoid the formation of platelets, the composition of the PDMA hydrogel was varied using ionic additives, as ionic groups in the polymer network show strong interactions with iron ions.[61–64] Hence, the influence of carboxylate group containing hydrogel networks on the precipitation of iron salts might be a way to obtain finer structures of the precipitated $FeCO_3$, which might lead to better energy dissipation and higher fracture toughness of the

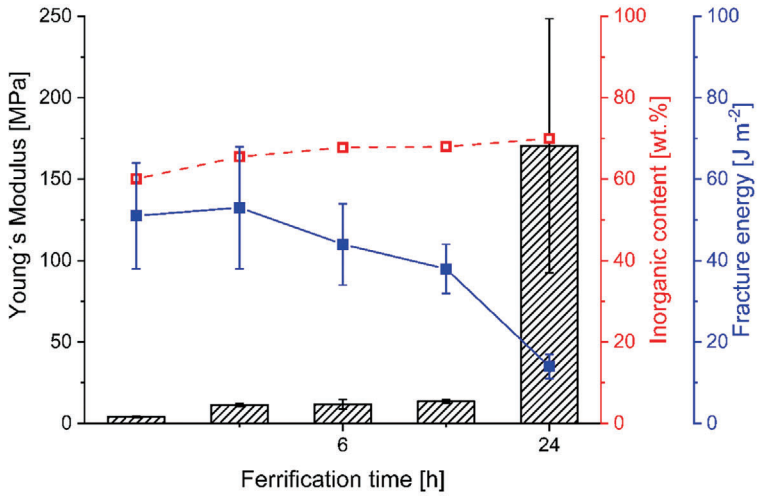

Network	Γ [J/m²]	E [MPa]	σ [MPa]
PDMA-*l*-TEG	14 ± 3	170 ± 78	0.3 ± 0.1

Figure 6. Fracture energy and Young´s Moduli of ferrified PDMA-*l*-TEG conetworks (1 wt% TEG, 1 wt% urease) after ferrification in a TEA buffered (0.2 M, pH 7.5) aqueous solution of $FeCl_2 \cdot 4H_2O$ (53.9 g L^{-1}) and urea (10 g L^{-1}), at 60 °C 24 h and of PAam-*l*-MBA conetworks (0.06 wt% MBA, 1 wt% urease) after ferrification in a TEA buffered (0.2 M, pH 9.3) aqueous solution of $FeCl_2 \cdot 4H_2O$ (53.9 g L^{-1}) and urea (10 g L^{-1}), at 60 °C 24 h. Young´s Modulus (black), fracture energy (blue), and inorganic weight content (red) of ferrified PDMA-*l*-TEG conetworks (1 wt% TEG, 1 wt% urease) after ferrification in a TEA buffered (0.2 M, pH 7.5) aqueous solution of $FeCl_2 \cdot 4H_2O$ (53.9 g L^{-1}) and urea (10 g L^{-1}) at 60 °C after 2–24 h.

Table 1. Swelling ratio, inorganic weight content, fracture energy, Young´s Modulus and tensile strength of PDMA-*l*-TEG networks (1 wt% TEG, 1 wt% urease) after ferrification in a TEA buffered (0.2 M, pH 7.5) aqueous solution of $FeCl_2$ (53.9 g L^{-1}) and urea (10 g L^{-1}), at 20 to 60 °C for 24 h.

Temperature [°C]	S	wt_{Inorg}%	E [MPa]	Γ [J m^{-2}]	σ [MPa]
20	4.1	41	14 ± 9	38 ± 21	0.3 ± 0.1
30	3.0	52	18 ± 11	36 ± 17	0.3 ± 0.1
40	2.6	70	156 ± 57	18 ± 5	0.4 ± 0.2
50	2.7	69	169 ± 58	11 ± 7	0.4 ± 0.1
60	2.6	70	170 ± 78	14 ± 3	0.3 ± 0.1

$FeCO_3$ composite. One way, to incorporate ionic groups is the copolymerizing DMA with acrylic acid (AA) or with its sodium salt (sodium acrylate, SA) during network formation. The ratio between DMA and the additive monomer was continually varied, until the degree of ferrification decreased, which might occur due to inhibition of the immobilized enzyme or diffusion limitations. The respective inorganic contents and swelling ratios are summarized in Figure S4A,B (Supporting Information).

Even a small amount of 2.5 wt% of copolymerized AA leads to a drop of the inorganic content in urease-loaded PDMA-*l*-TEG to 10 wt_{Inorg} % (Figure S4A, Supporting Information), while Young´s Moduli as well as tensile strength showed no increase compared to the nonferrified material. The incorporation of SA into PDMA networks leads to inhomogenous and patchy ferrification.

As known from previous work, the activity loss of urease in the presence of sodium acrylate groups is less pronounced in polyacrylamide cross-linked by *N*,*N*'-methylenebisacrylamide hydrogels (PAAm-*l*-MBAm).[43] Therefore, the ferrification experiments were repeated with the PAAm-based hydrogel with varying amounts of copolymerized SA keeping all other parameters constant.

As seen in **Figure 7**, the different chemical structure of the hydrogel already influences the morphology of the precipitated $FeCO_3$ platelets. They become thinner (<50 nm) and less regularly sized compared to the platelets formed in PDMA-*l*-TEG (cf. Figures 2 and 7), while still mineralizing homogenously throughout the network (Figure 7A).

The addition of SA into PAAm-*l*-MBAm networks leads to a further significant change of the morphology of the precipitated $FeCO_3$ platelets. Whereas lower amounts of 10 wt_{SA}% result in platelets arranged in stacked clusters (**Figure 8**C), higher copolymerized amounts yield smaller platelets (≈100–200 nm in size, ≈10–20 nm thickness) and more homogenously dispersed nanocrystals throughout the hydrogel matrix (Figure 8D). This results in an increased stiffness of 341 ± 98 MPa and an increased strength of 2.2 ± 1.1 MPa, indicating strong interaction between the copolymerized ionic groups and the $FeCO_3$ nanoplatelets (Figure 8), which is further supported by the decreasing swelling ratio S of the networks from 2.2 at 10 wt_{SA}% to 1.4 at 50 wt_{SA}% (Figure S4B, Supporting Information). However, this also leads to severe embrittlement of the fully ferrified hydrogels under the given conditions. Homogenous precipitation throughout the network is not influenced by incorporation of SA (Figure 8B–E), and the formation of a ferrification front is still present.

We conclude from this that the incorporation of ionic groups has a strong influence on the precipitated inorganic iron carbonate phase and that the nanostructures can be reduced in size and distributed more homogeneously (Figure 8D,E) in the network if charged groups are present in the hydrogel matrix. Even though these modifications lead to stronger composites, the overall gain in fracture toughness of the precipitated material is negligible. Altogether, the precipitation of ordered platelets might greatly change the toughness of the material. As seen on the example of the air bubbles in Figure 3, it is generally possible to obtain such an alignment, but so far, realization of such an arrangement throughout the whole material was not successful.

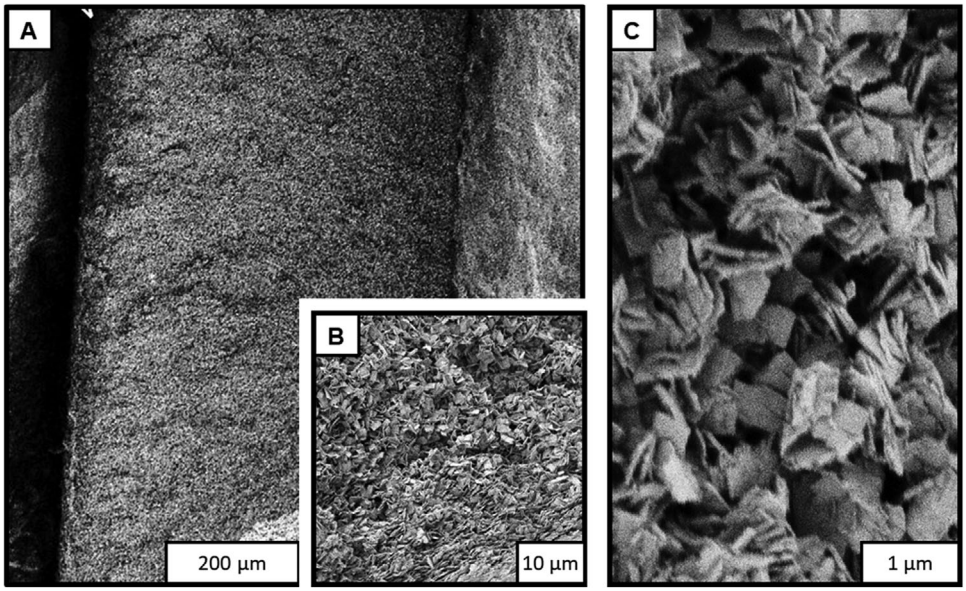

Figure 7. A–C) SEM-image of a PAAm-*l*-MBA cross-section (0.06 wt% MBA, 1 wt% urease) after ferrification in a TEA buffered (0.2 M, pH 9.3) aqueous solution of $FeCl_2 \bullet 4H_2O$ (53.9 g L^{-1}) and urea (10 g L^{-1}), at 60 °C 24 h. SEM-Images were taken in the middle of the network.

2.2. Alkaline Phosphatase-Induced Precipitation of Iron Phosphate

Another potentially useful iron salt that might be precipitated via EIM is iron phosphate. A viable enzyme that could be suited for this purpose is alkaline phosphatase (AP), which catalyzes the hydrolysis of glycerol phosphate, creating phosphate ions that can precipitate with iron ions present in the solution. Further, enzymatic precipitation of iron phosphate might be of interest for the design of new electrode materials, as the formation of metal phosphates takes place under mild conditions and ambient temperature and is less energy consuming compared to conventional iron phosphate production.[65]

Potential inorganic iron phosphate may exist as either Fe(II)- or Fe(III)-salts, thus it was investigated whether alkaline phosphatase is active in Fe(II)- and Fe(III)-containing solutions of glycerol phosphate. If active, the enzyme should precipitate insoluble iron phosphate. First, $FeCl_2 \bullet 4H_2O$ containing aqueous solutions of TEA and glycerol phosphate at different iron concentrations and pH values were mixed with alkaline phosphatase (0.4 mg per 100 mL). Only at a pH between 7.5 and 9.8 was formation of the pale green-blue solid observed, at $FeCl_2$ concentrations above 0.03 and below 0.33 M. The respective solutions of $FeCl_3$ did not show any precipitation in the whole pH range between 5 and 9.8 and at iron(III) ion concentrations of 0.03–0.33 M. Addition of $CaCl_2$ to these solutions revealed that alkaline phosphatase is inhibited at all concentrations by the Fe(III) ions, as no precipitation was observed after addition of $CaCl_2$ either.

To investigate whether enzymatic precipitation with AP in the presence of Fe(II) ions is also occurring within hydrogels, a PAAm-*l*-MBAm (0.06 wt% MBAm) network containing 0.4 wt% AP was given to the ferrification and incubated at 20 °C for 7 days. The hydrogel turned greenish cloudy after 24 h, as seen in **Figure 9**A, while control networks without the enzyme stayed transparent even after 7 days. SEM analysis of the ferrified networks revealed, that the ferrification leads to the formation of submicrometer structures, which are evenly distributed and precipitated throughout the hydrogel (Figure 9A,B). Irrespective of the investigated position within the network, nanospheres formed with diameters of ≈100–200 nm, which seem to be partially covered by polymer matrix. The particles do not change in diameter across the hydrogel, indicating a homogeneous mineralization throughout the material. Also, no local ferrification, as was found for the urease system (Figure 5), could be observed for the AP-induced precipitation.

Further investigations on the spherical precipitant inside the hydrogels reveal amorphous nanostructures, as SAED-measurements shows that the precipitated material is missing any reflexes that might be attributed to crystalline modifications (Figure 9D). TEM-EDX measurements reveal the presence of iron, oxygen and phosphorus, indicating, that the precipitated material is indeed, amorphous iron phosphate (Figure 9E). Judging from the greenish color, it is most likely iron(II) phosphate, as the corresponding mineral vivianite is of similar dark green coloration when partially oxidized.[66] The salt is most likely that of iron(II), as iron(III) ions showed strong inhibitory properties for the enzyme AP and would not allow the formation of a precipitate in solution even at very low concentrations. Thus, contrary to the precipitation of crystalline iron carbonate, iron phosphate precipitates as an amorphous and spherical nanostructured material during ferrification. The ferrified PAAm-*l*-MBAm hydrogel is composed of 80 wt% of inorganic material, with a swelling ratio S of 3.1. Ferrification at higher concentrations of $FeCl_2 \bullet 4H_2O$ with 0.22 and 0.33 mol L^{-1} led to decreasing inorganic content of 74.7 and 72.7 wt%, respectively. The amorphous character of the precipitated iron phosphate is of special interest, as this material might be promising for use as amorphous electrodes.[50]

The AP-ferrified PAAm-hydrogel with 80 wt% inorganic content is tougher (201 ± 66 J m^{-2}) and stiffer (122 ± 31 MPa) than hydrogels ferrified at 0.22 and 0.33 mol L^{-1} $FeCl_2 \bullet 4H_2O$, which

Network	Γ [J/m²]	E [MPa]	σ [MPa]
PAAm-*l*-MBAm	57 ± 11	24 ± 11	0.4 ± 0.1
+ *10 wt.$_{SA}$%*	-	164 ± 75	0.6 ± 0.1
+ *20 wt.$_{SA}$%*	-	85 ± 9	0.3 ± 0.1
+ *30 wt.$_{SA}$%*	-	42 ± 17	0.7 ± 0.1
+ *40 wt.$_{SA}$%*	-	341 ± 98	2.2 ± 1.1
+ *50 wt.$_{SA}$%*	-	275 ± 69	2.2 ± 0.3

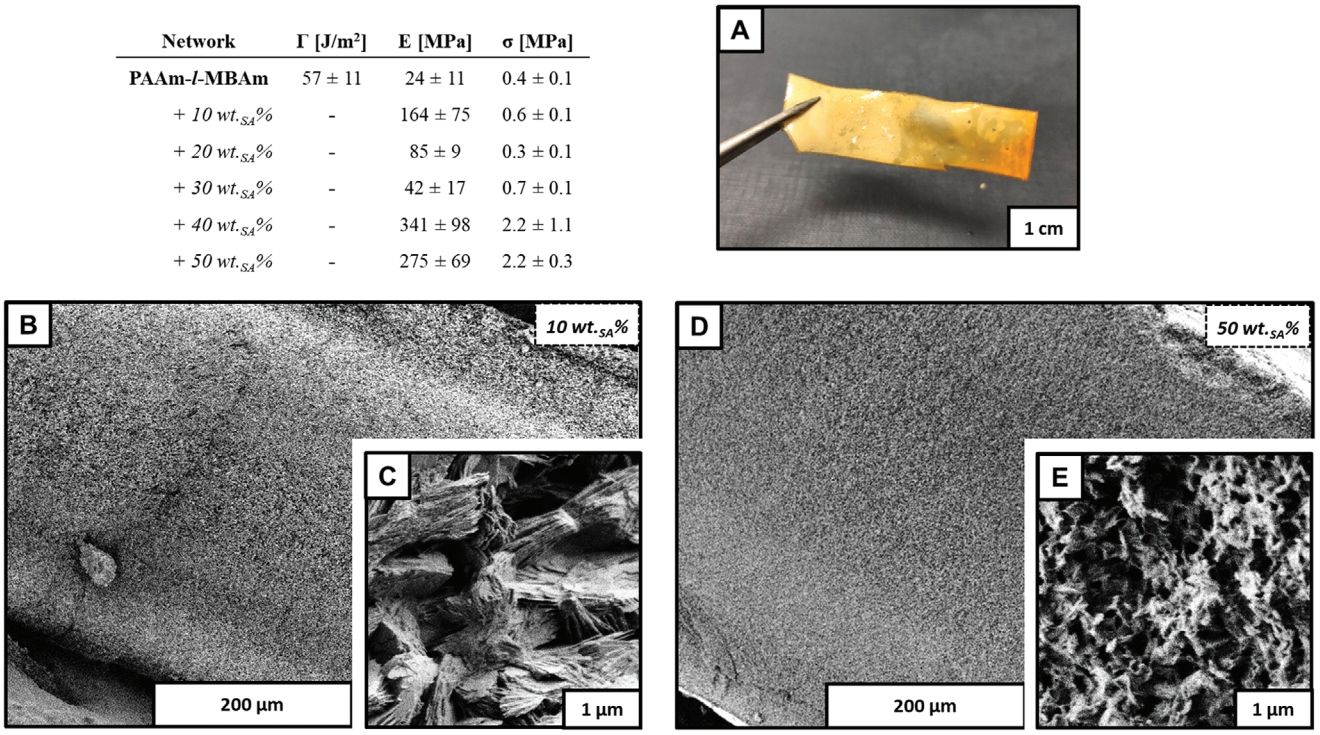

Figure 8. Fracture energy, Young´s Modulus and tensile strength of PAAm-*l*-MBA networks with different sodium acrylate (SA) content (0–50 wt_{SA}%, 0.06 wt% MBA, 1 wt% urease) after ferrification in a TEA buffered (0.2 M, pH 7.5) aqueous solution of $FeCl_2$ (53.9 g L^{-1}) and urea (10 g L^{-1}), at 60 °C 24 h. Photograph of a PAAm-*l*-MBA network with 10 wt% sodium acrylate A) and SEM-images of the exemplary network cross sections of PAAm-*l*-MBA networks with sodium acrylate content of 10 B,C) and 50 D,E) wt% after ferrification is also shown.

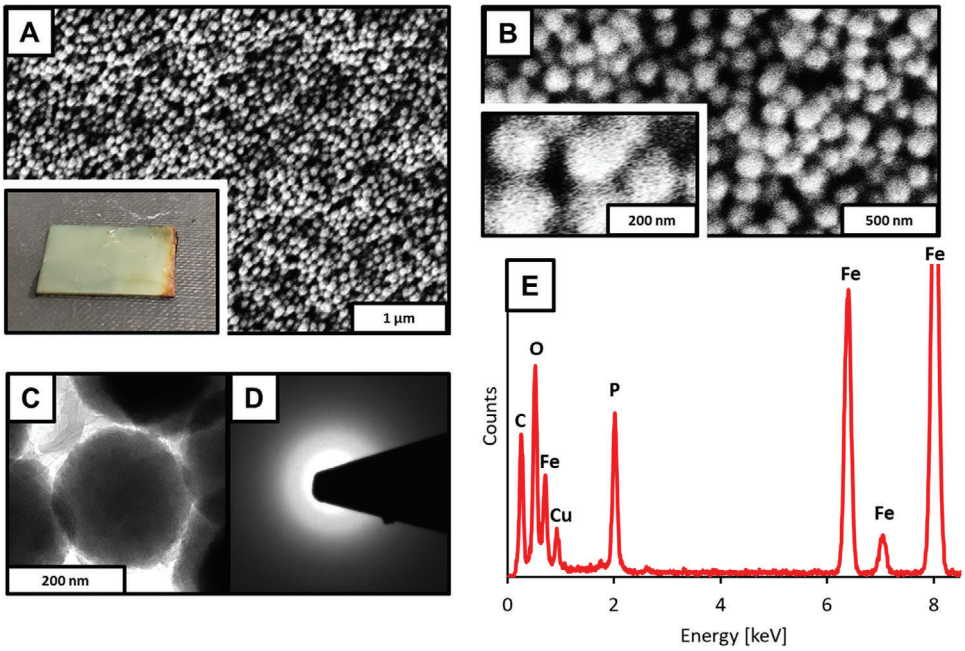

Figure 9. SEM-images of a PAAm-*l*-MBAm cross-section (0.06 wt% MBA, 0.4 wt% alkaline phosphatase) at different magnifications after ferrification in a TEA buffered (0.2 M, pH 9.8) aqueous solution of $FeCl_2$•$4H_2O$ (22.5 g L^{-1}) and NaGP (11.7 g L^{-1}) at 20 °C for 7 d. C) Exemplary TEM image of spherical micro structures grown in the ferrified PAAm-*l*-MBAm conetwork with D) typical SAED image. E) Typical TEM-EDX measurement of a composite slice recorded on a copper grid. Images were taken in the middle of the film.

Network	Γ [J/m²]	E [MPa]	σ [MPa]
PAAm-*l*-MBAm	201 ± 66	122 ± 31	1.3 ± 0.4
+ *10 wt.$_{SA}$%*	56 ± 37	14 ± 8	0.3 ± 0.2
+ *20 wt.$_{SA}$%*	104 ± 56	12 ± 4	0.3 ± 0.1
+ *30 wt.$_{SA}$%*	217 ± 56	54 ± 11	0.5 ± 0.1
+ *40 wt.$_{SA}$%*	281 ± 49	74 ± 12	1.1 ± 0.2
+ *50 wt.$_{SA}$%*	401 ± 37	101 ± 14	1.0 ± 0.2

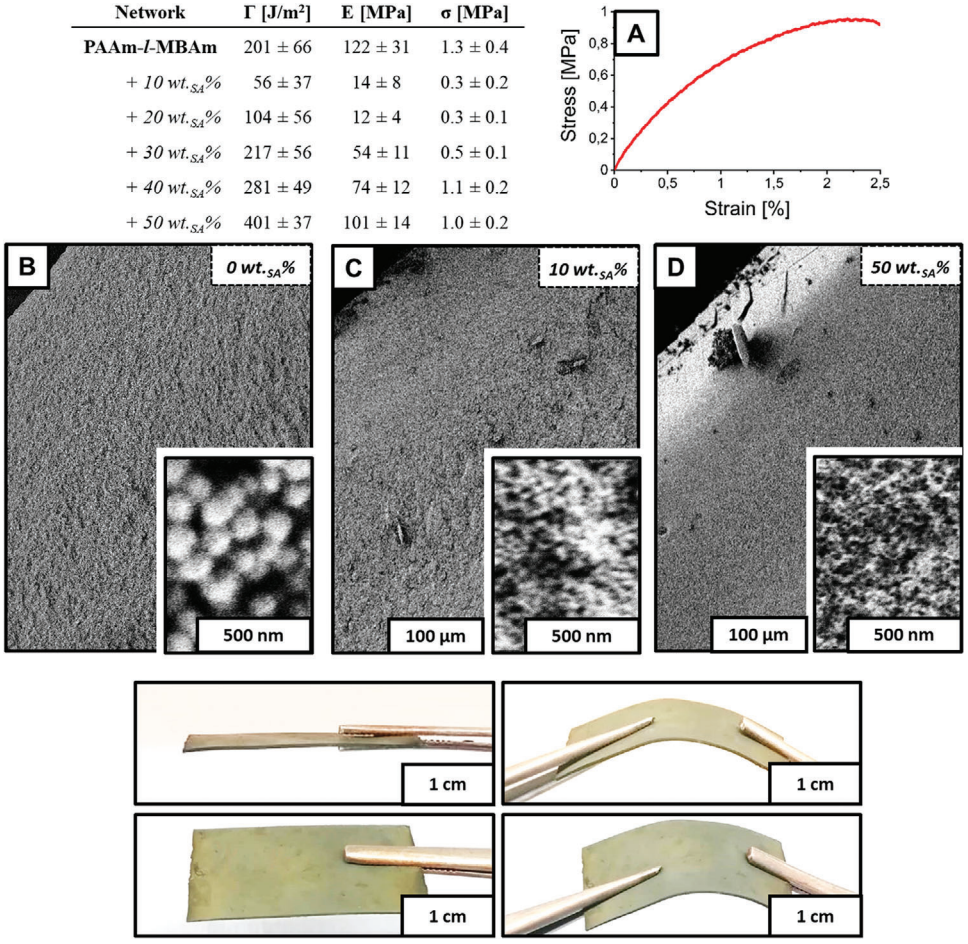

Figure 10. Fracture energy, Young´s Modulus and tensile strength of PAAm-*l*-MBA networks with different sodium acrylate (SA) content (0–50 wt_{SA}%, 0.06 wt% MBA, 0.4 wt% alkaline phosphatase) after ferrification in a TEA buffered (0.2 M, pH 9.8) aqueous solution of $FeCl_2 \cdot 4H_2O$ (22.5 g L^{-1}) and NaGP (11.7 g L^{-1}) at 20 °C for 7 d. Exemplary stress–strain curve of a PAAm-*l*-MBA network with 50 wt% sodium acrylate A) and SEM-images of the exemplary network cross sections of PAAm-*l*-MBA networks with sodium acrylate content of 0 B), 10 C), and 50 D) wt% after ferrification is also shown. Bottom pictures are shown to illustrate the flexibility of the ferrified PAAm-*l*-MBA networks with 40 wt% sodium acrylate

showed insignificant increase in Young´s Modulus (18 ± 7 and 11 ± 5 MPa, respectively). In order to further increase the flexibility of the organic–inorganic DNH, AAm was copolymerized with different amounts of sodium acrylate. As seen in **Figure 10**A, an increasing carboxylate content results in an increased toughness of the ferrified composites. Incorporation of more than 50 wt_{SA}% leads to patchy, inhomogeneous material. Adding ionic groups to the hydrogel matrix not only increases the mechanical properties of the materials most likely due to the improved adhesion between the organic and the inorganic phase, but also controls particle growth and influences the size of the precipitated nanostructures (Figure 10B–D), with homogenous precipitation throughout the network independent of the amount of copolymerized ionic monomer. Already 10 wt_{SA}% afford a finer structure of the precipitated iron(II) phosphate aggregates. The inorganic spheres show some 50 nm in diameter. Further increasing the SA content results in even smaller structures of 10–20 nm. This leads to a Young´s Modulus of 101 ± 14 MPa and a tensile strength of 1.0 ± 0.2 MPa, with the highest measured fracture energy of 401 ± 37 J m^{-2}, obtained for a ferrified PAAm-hydrogel containing 50 wt_{SA}% with respect to the monomer AAm (Figure 10A). Although the fracture energy is comparatively low for hydrogels mineralized by EIM, it does render the ferrified network flexible and bendable to some degree and significantly increases the fracture toughness of the functional ceramic itself (Figure 10), making it an interesting material for future research in regards to its use as flexible electronics. Thus, this example shows the potential of enzymatic mineralization to create tough functional ceramic materials. In order to avoid the brownish coloration of the surface areas, it is thinkable to use a reducing agent, such as ascorbic acid to cross-link the alkaline phosphate in future work.[67] Subsequent oxidation of the iron(II) salt might create the respective $FePO_4$, which is of importance as battery electrode material.

3. Conclusion

The aim of this work was to obtain bendable hydrogel composites highly filled with a functional iron ceramic material by means of enzymatic ferrification of hydrogels and deliberate softening

and toughening of ceramic components. Siderite could be precipitated urease-induced with up to 70 wt% within PDMA-*l*-TEG networks as platelets of some 60 nm in thickness, which are arranged isotropically within the hydrogel. However, this composite is very brittle and no variation of pH, temperature, mineralization time, network composition, or enzyme loading changed that. Interestingly, the siderite platelets showed significant parallel alignment toward a brick-and-mortar structure around gas bubbles formed in the hydrogel. Achieving such a structure throughout the entirety of the hydrogel might result in comparable toughness to highly ordered nacre.

The precipitation of amorphous iron(II) phosphate within a hydrogel was achieved by alkaline phosphatase-induced ferrification of a PAAm-*l*-MBAm. Copolymerization with sodium acrylate afforded finer structures, with the resulting O-I-DNH containing up to 80 wt_{Inorg}% of iron(II) phosphate, while being still flexible with Young´s Moduli of 101 ± 14 MPa, fracture energies of 401 ± 37 J m^{-2} and tensile strengths of 1.0 ± 0.2 MPa. This makes ferrified iron(II) phosphate based materials an interesting candidate for bendable batteries. The intercalation of lithium ions into the flexible iron phosphate for the synthesis of amorphous $LiFePO_4$ composites is of high interest and will be addressed in future studies.

4. Experimental Section

Materials: *N*,*N*-dimethyl acrylamide (DMA) with a purity of 99% and acrylic acid with a purity of 99% was obtained from Merck. The monomers were distilled, stored at −25 °C under an argon atmosphere, and used within the next 2 weeks. Acrylamide (AAm) with a purity of 99%, *N*,*N*-methylenebisacrylamide (MBAm) of 99% purity and triethylene glycol dimethacrylate (TEG) with a purity of 95% were obtained from Merck and used without further purification. The photoinitiators Irgacure 2959 and Irgacure 651 were supplied by TCI Europe and by Ciba Specialty Chemicals, respectively. Alkaline phosphatase from calf intestine with an activity of 36.7 U mg^{-1} was purchased from AppliChem and stored at −25 °C. The alkaline phosphatase formulation contains about 40–50 wt% of protein. Urease from *Canavalia ensiformis* (Nr. 94 282) with an activity of 35 U mg^{-1} was purchased from Merck and stored at −25 °C. The urease formulation contains 10 wt% of protein. Urea, sodium glycerol phosphate, calcium chloride, and triethanolamine were obtained from Merck. A 32 wt% solution of HCl was purchased from VWR. $FeCl_2$•$4H_2O$ and $FeCl_3$ were purchased from VWR. All chemicals were of analytical grade or purer and used without further purification if not noted otherwise.

Preparation of Buffer and Ferrification Solution for Alkaline Phosphatase: A 0.2 M TEA buffer solution (29.84 g TEA in 1000 mL water), made from bidistilled and degassed water, was adjusted to a pH of 9.8 using an aqueous 1 M HCl solution. The ferrification solution was formulated by dissolving 11.7 g NaGP and 22.5 g $FeCl_2$•$4H_2O$ in 900 mL of the buffer solution. Then the TEA buffer was added to fill the solution up to 1000 mL (final concentrations 11.7 g L^{-1} $FeCl_2$•$4H_2O$ and 22.5 g L^{-1} NaGP, respectively).

Preparation of Buffer and Ferrification Solution for Urease: A 0.2 M TEA buffer solution (29.84 g TEA in 1000 mL water), made from bidistilled and degassed water, was adjusted to a pH of 7.5 or 9.3 (unless otherwise noted), using an aqueous 1 M HCl solution. The ferrification solution was formulated by dissolving 53.9 g $FeCl_2$•$4H_2O$ and 10 g Urea in 900 mL of the buffer solution. Then the TEA buffer was added to fill the solution up to 1000 mL (final concentrations: 53.9 g L^{-1} $FeCl_2$•$4H_2O$ and 10 g L^{-1} urea).

Preparation of Polyglutaraldehyde Solution: A polyglutaraldehyde (PGL) solution was formulated using a previously described method.[68] Briefly, 10 mL of aqueous glutaraldehyde solution (50 wt%), 10 mL of pure water and 0.6 mL of 1 M NaOH solution were mixed in a vessel under constant stirring at room temperature to adjust the pH value to 10.5. After 30 min, 0.6 mL of 1 M HCl solution was added to neutralize the reaction mixture. Then, an aqueous 0.2 M TEA buffer (pH 9.8) was used to dilute the PGL solution to a concentration of 20 g L^{-1} (4.24 mL PGL solution, 45.76 mL TEA buffer).

Polymer Film Synthesis with Alkaline Phosphatase: Synthesis of polymer networks was carried out according to a previously published protocol.[45,47] First, 0.4 mg of the alkaline phosphatase formulation was dissolved in a mixture of 10 µL of 0.2 M TEA buffer solution and 10 µL of the polyglutaraldehyde solution.

DMA-Based Networks: A mixture of DMA and 1 mg TEG was added to a vessel. Optionally, up to 50 mg of the monomer was substituted with the additive monomer acrylic acid (AA). Then 0.5 mg of the photoinitiator Irgacure 651 and 20 µL of the alkaline phosphatase solution were added to the mixture.

AAm Conetworks: Two solutions were prepared by dissolving AAm (500 g L^{-1}) or MBAm (10 g L^{-1}) in pure water. Then, 200 µL (99.94 wt% monomer) of the AAm solution was added to a vessel. Optionally, up to 100 µL per 50 mg were substituted with up to 50 mg additive monomer sodium acrylate (SA, for every mg of additive monomer, 2 µL of degassed and bidistilled water was added to ensure solubility). Then, 6 µL (0.06 wt%) of the MBAm solution, 2 mg of the photo initiator Irgacure 2959 and 20 µL of the alkaline phosphatase solution were added to the mixture.

Polymer Film Synthesis with Urease: Synthesis of polymer networks was carried out according to previously published protocols.[42–44,46–47] First, 1 mg of the urease formulation was dissolved in 20 µL of the TEA buffer solution.

DMA-Based Networks: A mixture of DMA and 1 mg TEG was added to a vessel. Optionally, up to 50 mg of the monomer was substituted with the additive monomer acrylic acid (AA). Then 0.5 mg of the photoinitiator Irgacure 651 and 20 µL of the urease solution were added to the mixture.

AAm Conetworks: Two solutions were prepared by dissolving AAm (500 g L^{-1}) or MBAm (10 g L^{-1}) in pure water. Then, 200 µL (99.94 wt% monomer) of the AAm solution was added to a vessel. Optionally, up to 100 µL per 50 mg were substituted with up to 50 mg additive monomer sodium acrylate (SA). Then, 6 µL (0.06 wt%) of the MBAm solution, 2 mg of the photo initiator Irgacure 2959 and 20 µL of the urease solution were added to the mixture.

Polymerization: The whole monomer–initiator–enzyme mixture was poured onto an adhesive-tape-covered glass slide (1 × 3 $inch^2$) with distance holders of 300 µm and another slide was placed on top. Polymerization was carried out in an ultraviolet flash light chamber (Emmi-Nail Premium) at λ = 340 nm for 480 s (flipping the slide over every 120 s). Then, the glass slides were carefully separated and the formed polymer film (thickness 300 ± 30 µm) was either ferrified or stored until use at −25 °C.[42–47]

Ferrification: 200 mL of the Ferrification solution was poured into a closed Schott bottle containing one enzyme-loaded network (typical polymer to solution ratio of 1 mg 1 mL^{-1}). The immersed networks with immobilized alkaline phosphatase were incubated at 20 °C in a climate chamber for 7 d, while networks with immobilized urease were incubated at 20 °C in a climate chamber or at 60 °C using a heated water bath for 24 h. The resulting composite material was taken out after ferrification and thoroughly rinsed with and stored in pure water at 20 °C.

Analytical Methods: Analysis of the mineralized hydrogel was carried out analogously to previous publications.[42–47] The ferrified composite networks were broken in liquid nitrogen prior to further analysis. The fracture surfaces of the cross-sections were investigated by SEM. Samples were mounted on aluminum stubs with double-sided carbon tape and recorded using a Hitachi S-4500 SEM with field-emission gun and Oxford Link Isis-System. The acceleration voltage was set to 1 kV (10 kV for EDX) and the working distance to 8 mm (15 mm for EDX). TEM, EDX, and SAED images were acquired with a Talos F200X Thermo Fisher Scientific system operating at 200 kV. The samples were prepared by cutting slices of thickness of 50–100 nm of the dried composite using an ultra-microtome with a diamond blade (Leica Ultracut S), and then transferred onto a carbon grid. The XRD patterns were measured with Bruker D8 ADVANCE or Philips PW 1080 diffractometer using Cu-anodes. For these measurements, the ferrified composites were taped onto a sapphire glass slide using double-sided TESA adhesive tape. The inorganic proportion of the ferrified films

was determined with thermal gravimetric analysis (TGA; Netzsch STA 409 C) using sample sizes of 10–15 mg and a heating ramp of 10 °C min^{-1} up to 600 °C. To determine the inorganic proportion, the weight loss of the sample during pyrolysis was measured. Water evaporation occurred below 200 °C, while decomposition of organic content starts above this temperature. The difference between m_{dry} and $m_{combusted}$ was used to calculate the inorganic content $m_{Inorg.}$ with $wt_{Inorg.}$ [%] = $m_{combusted}$ x $m_{dry}{}^{-1}$ x 100.Stress–strain curves were recorded at room temperature using an Instron 3340 tensile tester with a cell with load 1 kN. Rectangular samples with typical dimensions of 5 × 10 mm[2] (width × length) were cut using a razor blade. The thickness of each sample was individually measured and was typically between 0.3 and 0.8 mm. The samples were mounted between the clamps with an initial distance of 10 mm. Sandpaper was used to prevent slippage of the samples between the grips. The experiment was performed at a crosshead speed of 5% min^{-1} until the sample fractured. Meanwhile the sample was permanently moistened with water using a spray can.

The fracture energy of the hydrated double network was determined as described in previous work.[69] At least three notched and three unnotched samples per composite (length 10 mm, width 5 mm, thickness 0.4–0.9 mm) were clamped in the Instron 3340 tensile tester (clamp-to-clamp distance 10 mm) and their stress–strain-curves were measured with a cross-head speed of 5% min^{-1}. The notched samples were prepared by cutting a notch with a length of 50% of the sample width by using a razor blade. These samples were used to determine the strain that is necessary to turn the notch into a running crack. The corresponding fracture energy (Γ, in J m^{-2}) of the unnotched samples was calculated as follows

$$\Gamma = l_c \times \int_0^{\epsilon_c} \sigma(\epsilon)\, d\epsilon \quad (1)$$

where σ is the stress (in MPa), ϵ is the strain (as a percentage), ϵ_c is the strain that results in fracture of notched samples (%), and l_c is the initial distance from clamp to clamp (in mm).

Swelling Behavior: The mass of the dried (m_{dry}) and the swollen ($m_{swollen}$) composites or hydrogels were measured. Swelling was performed in pure water at room temperature for 24 h. The swelling ratio (S) was calculated as follows: $S = m_{swollen}\, m_{dry}{}^{-1}$.

Supporting Information

Supporting Information is available from the Wiley Online Library or from the author.

Acknowledgements

The authors thank Ciba Specialty Chemicals (part of BASF) for providing Irgacure 651.

Open access funding enabled and organized by Projekt DEAL.

Conflict of Interest

The authors declare no conflict of interest.

Author Contributions

J.C.T. and M.M. designed the study and interpreted the results. M.M, T.H., E.C., and O.E.J. prepared the composites, performed TGA, FTIR, mechanic and swelling experiments, and took optical and SEM images. V.B. performed TEM, SAED, and EDX analysis. M.M established first enzymatic bulk precipitation of percolating amorphous iron phosphate and iron carbonate within hydrogels during his master thesis at the TU Dortmund. N.R. supervised M.M during his master thesis. J.C.T. and M.M. wrote the manuscript.

Data Availability Statement

The data that support the findings of this study are available in the Supporting Information of this article.

Keywords

amorphous iron phosphate, composite materials, double network hydrogels, enzyme-induced ferrification, iron carbonate

Received: January 21, 2022
Revised: March 15, 2022
Published online: April 15, 2022

[1] N. Bruns, W. Bannwarth, J. C. Tiller, *Biotechnol. Bioeng.* **2008**, *101*, 19.
[2] M. Hanko, N. Bruns, J. C. Tiller, J. Heinze, *Anal. Bioanal. Chem.* **2006**, *386*, 1273.
[3] C. Krumm, S. Konieczny, G. J. Dropalla, M. Milbradt, J. C. Tiller, *Macromolecules* **2013**, *46*, 3234.
[4] I. Sittko, K. Kremser, M. Roth, S. Kuehne, S. Stuhr, J. C. Tiller, *Polymer* **2015**, *64*, 122.
[5] I. Schoenfeld, S. Dech, B. Ryabenky, B. Daniel, B. Glowacki, R. Ladisch, J. C. Tiller, *Biotechnol. Bioeng.* **2013**, *110*, 2333.
[6] G. Savin, N. Bruns, Y. Thomann, J. C. Tiller, *Macromolecules* **2005**, *38*, 7536.
[7] N. Bruns, J. C. Tiller, *Macromolecules* **2006**, *39*, 4386.
[8] M. Hanko, N. Bruns, S. Rentmeister, J. C. Tiller, J. Heinze, *Anal. Chem.* **2006**, *78*, 6376.
[9] A. Strassburg, J. Petranowitsch, F. Paetzold, C. Krumm, E. Peter, M. Meuris, M. Köller, J. C. Tiller, *ACS Appl. Mater. Interfaces* **2017**, *9*, 36573.
[10] Q. Chen, H. Chen, L. Zhu, J. Zheng, *J. Mater. Chem. B* **2015**, *3*, 3654.
[11] J. P. Gong, *Soft Matter* **2010**, *6*, 2583.
[12] J. P. Gong, Y. Katsuyama, T. Kurokawa, Y. Osada, *Adv. Mater.* **2003**, *15*, 1155.
[13] A. Strassburg, J. Petranowitsch, F. Paetzold, C. Krumm, E. Peter, M. Meuris, M. Köller, J. C. Tiller, *ACS Appl. Mater. Interfaces* **2017**, *9*, 36573.
[14] P. L. Chandran, F. Horkay, *Acta Biomater.* **2012**, *8*, 3.
[15] A. J. Sophia Fox, A. Bedi, S. A. Rodeo, *Sports Health* **2009**, *1*, 461.
[16] F. Nudelman, B. A. Gotliv, L. Addadi, S. Weiner, *J. Struct. Biol.* **2006**, *153*, 176.
[17] M. A. Meyers, A. Y.-M. Lin, P.-Y. Chen, J. Muyco, M. Chen, P.-Y. Muyco, *J. Mech. Behav. Biomed. Mater.* **2008**, *1*, 76.
[18] F. Barthelat, H. Tang, P. Zavattieri, C. Li, H. Espinosa, *J. Mech. Phys. Solids* **2007**, *55*, 306.
[19] H.-L. Gao, S.-M. Chen, L.-B. Mao, Z.-Q. Song, H.-B. Yao, H. Cölfen, X.-S. Luo, F. Zhang, Z. Pan, Y.-F. Meng, Y. Ni, S.-H. Yu, *Nat. Commun.* **2017**, *8*, 287.
[20] L.-B. Mao, H.-L. Gao, H.-B. Yao, L. Liu, H. Cölfen, G. Liu, S.-M. Chen, S.-K. Li, Y.-X. Yan, Y.-Y. Liu, S.-H. Yu, *Science* **2016**, *354*, 107.
[21] G. Du, A. Mao, J. Yu, J. Hou, N. Zhao, J. Han, Q. Zhao, W. Gao, T. Xie, H. Bai, *Nat. Commun.* **2019**, *10*, 800.
[22] P. Das, J. M. Malho, K. Rahimi, F. H. Schacher, B. Wang, D. E. Demco, A. Walther, *Nat. Commun.* **2015**, *6*, 5967.
[23] F. C. Meldrum, *Int. Mater. Rev.* **2003**, *48*, 187.
[24] E. Asenath-Smith, H. Li, E. C. Keene, Z. W. Seh, L. A. Estroff, *Adv. Funct. Mater.* **2012**, *22*, 2891.
[25] H. Li, H. L. Xin, D. A. Muller, L. A. Estroff, *Science* **2009**, *326*, 1244.
[26] L. A. Estroff, L. Addadi, S. Weiner, A. D. Hamilton, *Org. Biomol. Chem.* **2004**, *2*, 137.
[27] N. Nassif, N. Pinna, N. Gehrke, M. Antonietti, C. Jäger, H. Cölfen, *Proc. Natl. Acad. Sci. USA* **2005**, *102*, 12653.

[28] O. Grassmann, P. Löbmann, *Biomaterials* **2004**, *25*, 277.
[29] I. Sethmann, U. Helbig, G. Wörheide, *CrystEngComm* **2007**, *9*, 1262.
[30] N. Shi, G. Yin, M. Han, Z. Xu, *Colloids Surf., B* **2008**, *66*, 84.
[31] N. H. Munro, D. W. Green, A. Dangerfield, K. M. Mcgrath, *Dalton Trans.* **2011**, *40*, 9259.
[32] N. Martin, G. Youssef, *J. Mech. Behav. Biomed. Mater.* **2018**, *85*, 194.
[33] A. M. Jordan, S.-E. Kim, K. Van de Voorde, J. K. Pokorski, L. T. J. Korley, *ACS Biomater. Sci. Eng.* **2017**, *3*, 1869.
[34] A. Agrawal, N. Rahbar, P. D. Calvert, *Acta Biomater.* **2013**, *9*, 5313.
[35] K. Fukao, K. Tanaka, R. Kiyama, T. Nonoyama, J. P. Gong, *J. Mater. Chem. B* **2020**, *8*, 5184.
[36] G. Gao, G. Du, Y. Cheng, J. Fu, *J. Mater. Chem. B* **2014**, *2*, 1539.
[37] I. K. Han, T. Chung, J. Han, Y. S. Kim, *Nano Convergence* **2019**, *6*, 18.
[38] K. Haraguchi, H.-J. Li, *Macromolecules* **2006**, *39*, 1898.
[39] Q. Wang, R. Hou, Y. Cheng, J. Fu, *Soft Matter* **2012**, *8*, 6048.
[40] L. Yu, D. Wang, Y. Tan, J. Du, Z. Xiao, R. Wu, S. Xu, J. Huang, *Appl. Clay Sci.* **2018**, *156*, 53.
[41] M. Takafuji, M. A. Alam, H. Goto, H. Ihara, *J. Colloid Interface Sci.* **2015**, *455*, 32.
[42] M. Milovanovic, M. T. Unruh, V. Brandt, J. C. Tiller, *J. Colloid Interface Sci.* **2020**, *579*, 357.
[43] M. Milovanovic, L. Mihailowitsch, M. Santhirasegaran, V. Brandt, J. C. Tiller, *J. Mater. Sci.* **2021**, *56*, 15299.
[44] N. Rauner, L. Buenger, S. Schuller, J. C. Tiller, *Macromol. Rapid Commun.* **2015**, *36*, 224.
[45] N. Rauner, M. Meuris, M. Zoric, J. C. Tiller, *Nature* **2017**, *543*, 407.
[46] N. Rauner, M. Meuris, S. Dech, J. Godde, J. C. Tiller, *Acta Biomater.* **2014**, *10*, 3942.
[47] M. Milovanovic, N. Isselbaecher, V. Brandt, J. C. Tiller, *Chem. Mater.* **2021**, *33*, 8312.
[48] X. Ren, K. Turcheniuk, D. Lewis, W. Fu, A. Magasinski, M. W. Schauer, G. Yushin, *Small* **2018**, *14*, 1703425.
[49] M. Ai, K. Ohdan, *J. Mol. Catal. A: Chem.* **2000**, *159*, 19.
[50] V. Mathew, S. Kim, J. Kang, J. Gim, J. Song, J. P. Baboo, W. Park, D. Ahn, J. Han, L. Gu, Y. Wang, Y.-S. Hu, Y.-K. Sun, J. Kim, *NPG Asia Mater.* **2014**, *6*, e138.
[51] S. Zhao, Y. Yu, S. Wei, Y. Wang, C. Zhao, R. Liu, Q. Shen, *J. Power Sources* **2014**, *253*, 251.
[52] W. H. R. Shaw, D. N. Raval, *J. Am. Chem. Soc.* **1961**, *83*, 3184.
[53] F. J. Millero, W. Yao, J. Aicher, *Mar. Chem.* **1995**, *50*, 21.
[54] H. Bai, F. Walsh, B. Gludovatz, B. Delattre, C. Huang, Y. Chen, A. P. Tomsia, R. O. Ritchie, *Adv. Mater.* **2016**, *28*, 50.
[55] D. Ji, S. Choi, J. Kim, *Small* **2018**, *14*, 1801042.
[56] M. Y. Nassar, I. S. Ahmed, T. Y. Mohamed, M. Khatab, *RSC Adv.* **2016**, *6*, 20001.
[57] D. L. Graf, *Am. Mineral.* **1961**, *46*, 1283.
[58] I. Azoulay, C. Rémazeilles, P.h. Refait, *Corros. Sci.* **2012**, *58*, 229.
[59] T. Yasui, E. Kamio, H. Matsuyama, *Langmuir* **2018**, *34*, 10622.
[60] E. Kamio, T. Yasui, Y. Iida, J. P. Gong, H. Matsuyama, *Adv. Mater.* **2017**, *29*, 1704118.
[61] Q. Chen, X. Yan, L. Zhu, H. Chen, B. Jiang, D. Wei, L. Huang, J. Yang, B. Liu, J. Zheng, *Chem. Mater.* **2016**, *28*, 5710.
[62] S. Y. Zheng, H. Ding, J. Qian, J. Yin, Z. L. Wu, Y. Song, Q. Zheng, *Macromolecules* **2016**, *49*, 9637.
[63] P. Lin, S. Ma, X. Wang, F. Zhou, *Adv. Mater.* **2015**, *27*, 2054.
[64] S. Y. Zheng, H. C. Yu, C. Yang, W. Hong, F. Zhu, J. Qian, Z. L. Wu, Q. Zheng, *Mater. Today Phys.* **2020**, *13*, 100202.
[65] T. V. S. L. Satyavani, A. Srinivas Kumar, P. S. V. Subba Rao, *Int. J.* **2016**, *19*, 178.
[66] R. V. Gaines, *The System of Mineralogy of James Dwight Dana and Edward Salisbury Dana*, Wiley, New York **1997**.
[67] J. Tiller, P. Berlin, D. Klemm, *Biotechnol. Appl. Biochem.* **1999**, *30*, 155.
[68] A. Tanriseven, Z. Ölçer, *Biochem. Eng. J.* **2008**, *39*, 430.
[69] R. S. Rivlin, A. G. Thomas, *J. Polym. Sci.* **1953**, *10*, 291.

